Contents lists available at ScienceDirect

Applied Catalysis B: Environment and Energy

Heterointerface and crystallinity engineering of Ru/RuS2 dual co-catalysts for enhanced photocatalytic hydrogen evolution

Xinyu Wang [a], Junhua You [b,*], Jiali Ren [a], Yanjun Xue [a], Jian Tian [a,*], Hangzhou Zhang [c,*]

[a] School of Materials Science and Engineering, Shandong University of Science and Technology, Qingdao 266590, China
[b] School of Materials Science and Engineering, Shenyang University of Technology, Shenyang 110870, China
[c] Department of Orthopedics; Joint Surgery and Sports Medicine, First Affiliated Hospital of China Medical University; Shenyang Sports Medicine Clinical Medical Research Center, Shenyang 110001, China

A B S T R A C T

In this paper, the Ru/RuS$_2$ nanoparticles as dual co-catalysts were self-assembled on the surface of g-C$_3$N$_4$ nanotubes (Ru/RuS$_2$/g-C$_3$N$_4$ NTs) for photocatalytic H$_2$ production. The Ru/RuS$_2$/g-C$_3$N$_4$ NTs showed greatly enhanced photocatalytic H$_2$ production activity (1409 μmol·g^{-1}·h^{-1}), 1.16 times of RuS$_2$/g-C$_3$N$_4$ NTs (1212 μmol·h^{-1}·g^{-1}), 10.51 times of Ru/g-C$_3$N$_4$ NTs (134 μmol·g^{-1}·h^{-1}), and 82.88 times of the pure g-C$_3$N$_4$ NTs (17 μmol·g^{-1}·h^{-1}). Besides, the apparent quantum yield value (AQE) of Ru/RuS$_2$/g-C$_3$N$_4$ NTs is 3.92% at 370 nm. Ru/RuS$_2$ as dual co-catalysts are self-assembled on the surface of g-C$_3$N$_4$ NTs and show strong electronic synergistic interaction between the interfaces, reduce ΔG_{H*} of RuS$_2$ and desorption energy of Ru, and promote the selectivity and activity of HER kinetically and thermodynamically respectively, which exhibits higher photogenerated carrier concentration and lower charge migration resistance than RuS$_2$ and Ru, showing the synergistic effect to facilitate the generation and migration of carriers and provides active sites for photocatalysis.

1. Introduction

The fast-depleting fossil fuels, increasing demand for energy from industrial development and population growth have prompted scientific research and policy formulation to promote the development of renewable and clean energy [1–3]. The report of Carbon Dioxide Emissions in 2022 from the International Energy Agency (IEA) unveil that the global CO$_2$ emissions from fossil fuels combustion are about 36.8 Gt in 2022, while the total amount of CO$_2$ are prevented by increased the clean energy technologies like electric vehicles, heat pumps, and renewables, is about 550 Mt, less than 1.5% [4,5]. Global warming and several other related environmental hazards have raised international concerns that drive the research on the development of new energy technologies.

Hydrogen (H$_2$) energy is the most ideal alternative energy to replace fossil energy for the high energy density and no other pollutants in the combustion process, but the main way to produce H$_2$ at present is burning fossil fuels to generate electricity and electrolyze water to produce hydrogen [6,7]. Honda K. and Fujishima A. discovered that TiO$_2$ can be used to split water into H$_2$ under light in 1972 [8], then photocatalytic H$_2$ production without generating other pollutants has

been paid extensive attention to clean energy for improving earth energy and environmental problems [9,10]. A large number of photocatalysts have been designed and applied to photocatalytic hydrogen production in recent years, including nitrides (g-C$_3$N$_4$) [11–13], metal oxides (TiO$_2$) [14–17], oxyhalides (BiOBr) [18–20], and sulfides (CdS and ZnIn$_2$S$_4$) [21–23]. However, the rapid recombination of photogenerated holes and electrons, and the limited active sites of the catalytic material itself severely limit the application of photocatalytic hydrogen production.

Recent studies related to photocatalysis have shown that layered porous materials with more surface area might be the best candidate materials [24,25]. Graphitic carbon nitride (g-C$_3$N$_4$) is the most promising photocatalyst candidate due to its typical layered structure, physical and chemical stability, and appropriate band structure (2.7 eV) [26,27]. However, the photocatalytic activity of pure g-C$_3$N$_4$ is still far from applications due to the fast recombination of photoexcited holes and electrons. A great number of catalyst modification strategies have been proposed to enhance photocatalytic performance [28–30]. Recent studies have shown that rationally designing the morphology of catalyst materials can enhance light absorption, improve charge transport, and increase specific surface area and surface reaction sites, thereby improving its photocatalytic performance, such as nanosheets [31,32],

nanotubes [33,34], nanorods [35] and nanocages [36], etc. In addition, the co-catalyst strategy is generally considered an ideal way to enhance the photocatalytic H_2 production activity of semiconductor catalysts [37–39]. At present, noble metals are the most ideal co-catalysts for photocatalytic H_2 evolution reactions, such as Pt, Au and Pd, etc [40–45]. However, the scarcity and high cost limit the applications. Therefore, the development of co-catalysts prepared from lower cost elements has attracted extensive attention. The co-catalyst strategy can enhance the efficiency of photocatalytic hydrogen production as the co-catalyst could expand the light absorption range and provide active sites, thus improving the three important processes of light absorption, carrier transport, and surface reaction in the photocatalytic process, respectively, such as Pt/g-C$_3$N$_4$/TiO$_2$/IrO$_x$ [43], 1 T-WS$_2$/g-C$_3$N$_4$ [46] and CoS$_2$/g-C$_3$N$_4$ [40].

Ruthenium (Ru) and ruthenium sulfide (RuS$_2$) cocatalysts are used as effective substitutes for noble metals for the lower hydrogen binding free energy and lower cost. Firstly, according to the price survey of the tansoole drug platform, the price per gram of ruthenium chloride (RuCl$_3$, Adamas, ≥99.5%) as the raw material is about 29% of chloroplatinic acid hexahydrate (H$_2$PtCl$_6$·6 H$_2$O, Adamas, ≥99.9%), and the price per gram of metal Ru in the RuCl$_3$ is about 23% of Pt in H$_2$PtCl$_6$·6 H$_2$O. Secondly, relevant studies have shown that Ru possessed better hydrogen evolution reaction (HER) activity than Pt in alkaline environments [47–49] for it decreased the dissociation energy barrier of H-OH bond [50–55]. Zheng et al. reported that the dissociation energy barrier of H-OH bond of Ru is 0.41–0.51 eV, which is much lower than Pt (0.94 eV) [50]. Ye et al. proved that the HER performance of RuNCs/BNG was better than Pt/C in alkaline environments as the lower water dissociation energy barrier of Ru improved the alkaline HER [56]. However, Ru possessed strong hydrogen binding energy, and higher hydrogen desorption energy barrier proved by DFT calculations, which was not conducive to the hydrogen desorption, thus inhibiting HER kinetics [50,52,57,58]. Recently, RuS$_2$ as HER catalyst showed good performance as the hydrogen adsorption free energy of RuS$_2$ is similar to Pt [59–64]. Li et al. showed that RuS$_x$ nanoparticles supported on sulfur-doped graphene oxide possessed smaller overpotential and better carrier migration [60]. Zhu et al. showed that RuS$_2$ nanoparticles possessed enhanced HER activity in the alkaline environment [63]. Therefore, the coupling of Ru and RuS$_2$ to form a heterostructure as dual cocatalysts for the photocatalytic hydrogen evolution is expected to simultaneously optimize the energy of water dissociation and hydrogen adsorption. The two components Ru and RuS$_2$ serve as dual cocatalysts and can provide strong electronic synergistic interaction between the interfaces, which provides more active sites at the interface for photocatalytic hydrogen production. However, Ru/RuS$_2$ as dual co-catalysts to enhance photocatalytic hydrogen evolution performance has rarely been reported.

In this paper, the Ru/RuS$_2$ nanoparticles as dual co-catalysts were self-assembled on the surface of g-C$_3$N$_4$ nanotubes (Ru/RuS$_2$/g-C$_3$N$_4$ NTs) through the heat treatment and grinding self-assembly using RuCl$_3$, K$_2$S and dicyandiamide as raw material for photocatalytic hydrogen evolution. The Ru/RuS$_2$/g-C$_3$N$_4$ NTs showed greatly improved photocatalytic H$_2$ evolution activity (1409 μmol·h^{-1}·g^{-1}), 1.16 times of the RuS$_2$/g-C$_3$N$_4$ NTs (1212 μmol·g^{-1}·h^{-1}), 10.51 times of Ru/g-C$_3$N$_4$ NTs (134 μmol·g^{-1}·h^{-1}), and 82.88 times of the pure g-C$_3$N$_4$ NTs (17 μmol·g^{-1}·h^{-1}). Besides, the AQE of 20 mg Ru/RuS$_2$/g-C$_3$N$_4$ NTs is 3.92% at 370 nm. The tests and characterization results prove that g-C$_3$N$_4$ NTs with hexagonal porous morphology have a porous sheet-like internal structure, which is beneficial to increase the specific surface area, thereby increasing light absorption and facilitating electron and mass transport. The loading of Ru/RuS$_2$ as dual co-catalysts in the g-C$_3$N$_4$ NTs can extend the range of light absorption to visible light and near-infrared light regions, respectively, and provide the heterointerfaces as surface active sites to capture carriers to take part in the surface H$_2$ evolution reaction. The Ru/RuS$_2$ as dual co-catalysts are self-assembled on the surface of g-C$_3$N$_4$ NTs and show strong electronic synergistic interaction

between the interfaces, which exhibits higher photogenerated carrier concentration and lower charge migration resistance than RuS$_2$ and Ru, showing the synergistic effect to facilitate the generation and migration of carriers and provides active sites for surface reaction, then improving photocatalytic H$_2$ evolution.

2. Experimental section

2.1. Materials

The 1-propanol (C$_3$H$_8$O, ≥ 99.5%), dicyandiamide (C$_2$H$_4$N$_4$, ≥ 99.0%), hexane (C$_6$H$_{14}$, ≥ 97.0%), ethanol (C$_2$H$_5$OH, ≥ 99.7%), triethanolamine (TEOA) (C$_6$H$_{15}$NO$_3$, ≥ 99.0%), methyl alcohol (CH$_3$OH, ≥ 99.5%), lactic acid (C$_3$H$_6$O$_3$, ≥ 80.0%) and chloroplatinic acid hexahydrate (H$_2$PtCl$_6$·6 H$_2$O, ≥ 99.9%) were bought from Greagent. The lithium chloride (LiCl, ≥ 99.0%), potassium chloride (KCl, ≥ 99.0%) and ruthenium (III) chloride (RuCl$_3$, ≥ 99.5%) were bought from Adamas. The potassium sulfide anhydrous (K$_2$S, ≥ 95.0%) was bought from Aladdin. The deionized water was used in all tests, and all the chemical reagents were used without purification.

2.2. Preparation of bulk g-C$_3$N$_4$

For typical synthesis, the bulk g-C$_3$N$_4$ was obtained via one-step heat treatment in air atmosphere. Briefly, 2 g dicyandiamide was placed in a crucible with aluminum foil wrapped, and heated to 550 °C at the rate of 10 °C·min^{-1} for 4 h in air.

2.3. Preparation of g-C$_3$N$_4$ nanotubes (NTs)

The g-C$_3$N$_4$ NTs with hexagonal prism morphology were synthesized by hydrothermal and thermal treatments. Firstly, 5 mL DI water and 10 mL propanol were stirred thoroughly to form a mixed solution A. Secondly, 3 g dicyandiamide was added to the above-mentioned solution A, and stirred 30 min to form solution B. Then, solution B was added to a 50 mL stainless steel reactor with Teflon liner and heated to 180 °C for 4 h. And the precipitation was fully washed with water after the reactor was cooled to room temperature, and dried under vacuum at 60 °C for 6 h. Finally, dried precipitation was heated to 550 °C at 10 °C·min^{-1} for 4 h to obtain g-C$_3$N$_4$ NTs with hexagonal prism morphology. To compare the performance of the composite catalyst, 1 wt% Pt/g-C$_3$N$_4$ NTs (named g-C$_3$N$_4$ NTs/Pt) were obtained by adding 20 mg g-C$_3$N$_4$ NTs and 0.2 mg Pt from 0.193 M H$_2$PtCl$_6$·6 H$_2$O aqueous solution under 300 W Xe lamp with AM-1.5 filter for 1 h.

2.4. Preparation of Ru/RuS$_2$ nanoparticles (NPs)

Ru/RuS$_2$ NPs were synthesized by the melting salt method. 1.35 g LiCl and 1.65 g KCl were added to the mortar and ground to form the eutectic salt system in the glove box. Then, 1 mmol RuCl$_3$ and 4 mmol K$_2$S were added to the above eutectic salt in the mortar and thoroughly ground. Then, the above precursor was placed in the corundum boat in a tube furnace, and heated to 800 °C at a rate of 10 °C·min^{-1} under N$_2$ for 2 h. The obtained product was washed with deionized water, and dried for 6 h under vacuum to obtain Ru/RuS$_2$ NPs. Comparative samples of Ru, Ru/RuS$_2$-2, Ru/RuS$_2$-3, and RuS$_2$ were obtained by adjusting the ratio of RuCl$_3$ and K$_2$S to 1:1, 1:2, 1:3, and 1:5.

2.5. Preparation of Ru/RuS$_2$/g-C$_3$N$_4$ NTs

Ru/RuS$_2$/g-C$_3$N$_4$ NTs were synthesized by simple mechanical grinding method. 10 mg Ru/RuS$_2$ NPs, 90 mg g-C$_3$N$_4$ NTs, and 5 mL hexane were added into mortar and ground. Then 2 mL ethanol was added into the mortar and ground again. The solution was washed several times with ethanol before drying the final composite. The prepared composite was named Ru/RuS$_2$/g-C$_3$N$_4$ NTs (10 wt%). Similarly,

a series of composites containing different amounts of Ru/RuS$_2$ were obtained by adjusting the amount of Ru/RuS$_2$, named Ru/RuS$_2$/g-C$_3$N$_4$ NTs (1, 5 and 15 wt%). To compare the excellent catalytic performance of Ru/RuS$_2$/g-C$_3$N$_4$ NTs, three composites containing different co-catalysts with the same weight ratio, 10 mg Ru, Ru/RuS$_2$-2, Ru/RuS$_2$-3 and RuS$_2$, were obtained and named as Ru/g-C$_3$N$_4$ NTs (10 wt%), Ru/RuS$_2$-2/g-C$_3$N$_4$ NTs (10 wt%), Ru/RuS$_2$-3/g-C$_3$N$_4$ NTs (10 wt%) and RuS$_2$/g-C$_3$N$_4$ NTs (10 wt%).

2.6. Characterization

The X-ray diffraction (XRD) data was collected by the Rigaku Utima IV. X-ray photoelectron spectroscopy (XPS) data was collected by Thermo Scientific ESCALAB Xi+ instrument with Al K$_\alpha$, and all the XPS data was referenced with the C 1 s peak at 284.8 eV. The data of transmission electron microscope (TEM) with energy dispersive spectrometer (EDS), and scanning electron microscope (SEM) were tested by FEI Talos F200X and Apreo S HiVac instruments to characterize the nanostructure and morphology of the catalyst. The data of diffuse reflectance spectra (DRS) was tested by Hitachi UH4150. The photoluminescence (PL) data was tested by FLS980. The surface photovoltage (SPV) measurements were carried out on a surface photovoltage spectroscope (CEL-SPS1000) under ambient conditions.

2.7. Photoelectrochemical test

The transient photocurrent (TPC), electrochemical impedance spectrum (EIS), linear sweep voltammetry (LSV), and Mott-Schottky (MS) tests were collected on CHI 660D workstation with the three-electrode system in the 0.5 M Na$_2$SO$_4$ solution, including Ag/AgCl, samples and Pt wire and reference, work and counter electrodes. The frequency range of the EIS test was $10^{-2} \sim 10^5$ Hz. The frequency range of the MS test were 1000, 2000 and 3000 Hz.

2.8. Photocatalytic activity test

The photocatalytic activity was tested in the 50 mL system containing 10 mg catalysts and 20 vol% TEOA aqueous solution in 150 mL photoreactor. The 300 W Xe lamp with AM-1.5 filter and gas chromatograph (GC-7920) were used as light source and product characterization. The AQE was tested in the same conditions and calculated via the equation as follows:

$$AQE = \frac{number\ of\ evolved\ H_2\ molecules\ \times 2}{number\ of\ incident\ photons} \times 100\% \quad (1)$$

3. Results and discussion

The g-C$_3$N$_4$ nanotubes (NTs) were synthesized by solvothermal and heat treatment using dicyandiamide as raw materials (Scheme 1). The Ru/RuS$_2$ was prepared by the melting salt method using RuCl$_3$ and K$_2$S as raw materials (Scheme 2). The Ru/RuS$_2$/g-C$_3$N$_4$ NTs composites were prepared by the grinding method (Scheme 3).

X-ray diffraction (XRD) (Fig. 1a and b) was used to characterize the different Ru/RuS$_2$ products obtained by adjusting the ratio of Ru and S elements during the eutectic salt method. As shown in the gray curve in Fig. 1a, the peaks at 38.4°, 42.2°, 44.0°, 58.3°, 69.4° and 78.4° are

attributed to the (100), (002), (101), (102), (110) and (103) crystal planes of hexagonal Ru (PDF#06–0663), respectively [65]. And the green curve in Fig. 1a also shows that the peaks at 27.5°, 31.9°, 35.8°, 39.3°, 45.7°, 54.2°, 56.8°, 59.3°, 61.8°, 73.5° and 75.8° are corresponding to the (111), (200), (210), (211), (220), (311), (222), (230), (321), (331) and (420) crystal planes of cubic RuS$_2$ (PDF#19–1107), respectively. It is worth noting that K$_2$S plays a reducing role to obtain pure phase metal Ru when the K$_2$S content is low ($n_{RuCl3}:n_{K2S} = 1$). However, K$_2$S mainly plays a sulfidation role to obtain pure phase RuS$_2$ when the K$_2$S content is excess ($n_{RuCl3}:n_{K2S} = 1:5$) [66]. The dual effects of reduction and sulfidation of K$_2$S are key to obtaining different phase compositions as the RuCl$_3$/K$_2$S ratio changes. The synthesis of Ru/RuS$_2$-2, Ru/RuS$_2$-3 and Ru/RuS$_2$-4 heterostructures with different RuCl$_3$/K$_2$S ratios ($n_{RuCl3}:n_{K2S} = 1:2, 1:3$ and $1:4$) also prove the dual effects of reduction and sulfidation of K$_2$S. It can be seen from Fig. 1a that the (101) main peak of Ru gradually weakens and disappears, and the (200) main peak of RuS$_2$ gradually strengthens from none with the increase of K$_2$S, indicating that RuCl$_3$ is almost sulfurized by K$_2$S to form pure phase RuS$_2$ with the increase of K$_2$S. The key Ru/RuS$_2$-4 had the weaker peaks of metallic Ru in Fig. 1a, showing improved catalytic performance. Unless otherwise stated, Ru/RuS$_2$-4 was used as the main research object and named Ru/RuS$_2$.

The specific characterizations of phase of g-C$_3$N$_4$ NTs and Ru/RuS$_2$/ g-C$_3$N$_4$ NTs (containing 1, 5, 10 and 15 wt% of Ru/RuS$_2$, respectively) were also characterized via XRD as shown in Fig. 1b. The XRD pattern of g-C$_3$N$_4$ NTs shows two diffraction peaks at 27.7° and 13.3°, corresponding to (002) and (100) planes of g-C$_3$N$_4$ from the planar stacking and the periodic stacking of heptazine structure, respectively [67]. The XRD pattern of Ru/RuS$_2$ shows the main diffraction peaks of RuS$_2$ and the weaker peaks of metallic Ru, which is attributed to the main sulfidation and a small amount of reduction of K$_2$S. The diffraction peaks of Ru/RuS$_2$ gradually strengthen and the peak of g-C$_3$N$_4$ NTs gradually weakens as the loading ratio of Ru/RuS$_2$ increases from 1 wt% to 15 wt %, proving that Ru/RuS$_2$ is successfully loaded on g-C$_3$N$_4$ NTs.

Survey and high-resolution core-level XPS spectra were used to reveal the composition and chemical state of 10 wt% Ru/RuS$_2$/g-C$_3$N$_4$ NTs as shown in Figs. S1 and 1c-f. All the binding energy was calibrated using the reference to C 1 s at 284.80 eV. The survey XPS spectrum in Fig. S1 shows that Ru/RuS$_2$/g-C$_3$N$_4$ NTs are composed of C, N, Ru, S and O elements, and the atomic ratio of Ru: S is approximately 0.61: 1, corresponding to the phase percentage of Ru: RuS$_2$ is approximately 18.1%: 81.9%, which indicates that 10 wt% Ru/RuS$_2$/g-C$_3$N$_4$ NTs catalyst is actually composed of Ru/RuS$_2$ and g-C$_3$N$_4$. The high-resolution XPS of C 1 s of g-C$_3$N$_4$ NTs shows two binding energy peaks at 288.26 and 284.80 eV, attributing to the C atoms in N = C(-N$_2$) group and graphitic C-C/C=C bonds of g-C$_3$N$_4$ as shown in Fig. 1c [68]. And the XPS spectrum of N 1 s of g-C$_3$N$_4$ NTs can be deconvoled as three peaks at the binding energy of 398.72, 399.99 and 401.01 eV, corresponding to sp2 hybridized pyridine nitrogen (C-N = C), sp3 hybridized tertiary nitrogen (N-(C)$_3$) and C-NH$_X$ of g-C$_3$N$_4$ (Fig. 1d) [69]. The C-N = C, N-(C)$_3$, C-NH$_X$ and N = C(-N$_2$) peaks of N 1 s and C 1 s of 10 wt % Ru/RuS$_2$/g-C$_3$N$_4$ NTs are located at 288.37, 398.88, 400.22, and 401.10 eV, respectively, which shifts toward higher binding energy after the loading of Ru/RuS$_2$ as dual co-catalysts on g-C$_3$N$_4$ NTs, indicating that the ruthenium ion with a positive charge, acting as electron donor, is partially combined with the nitrogen, and provides electrons to transfer from g-C$_3$N$_4$ NTs to Ru/RuS$_2$. The synergistic effect of charge
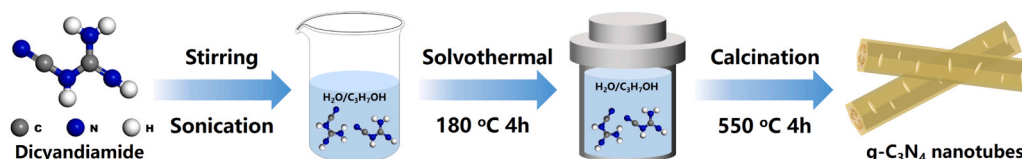
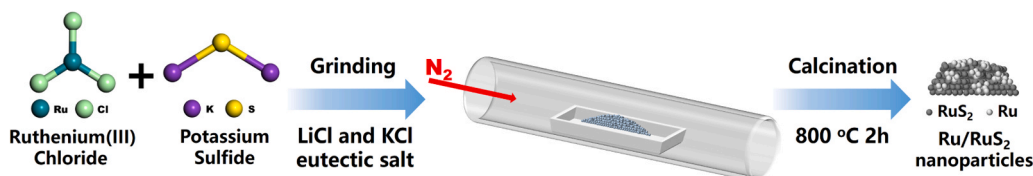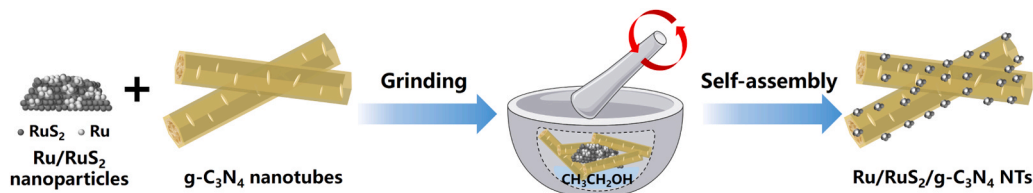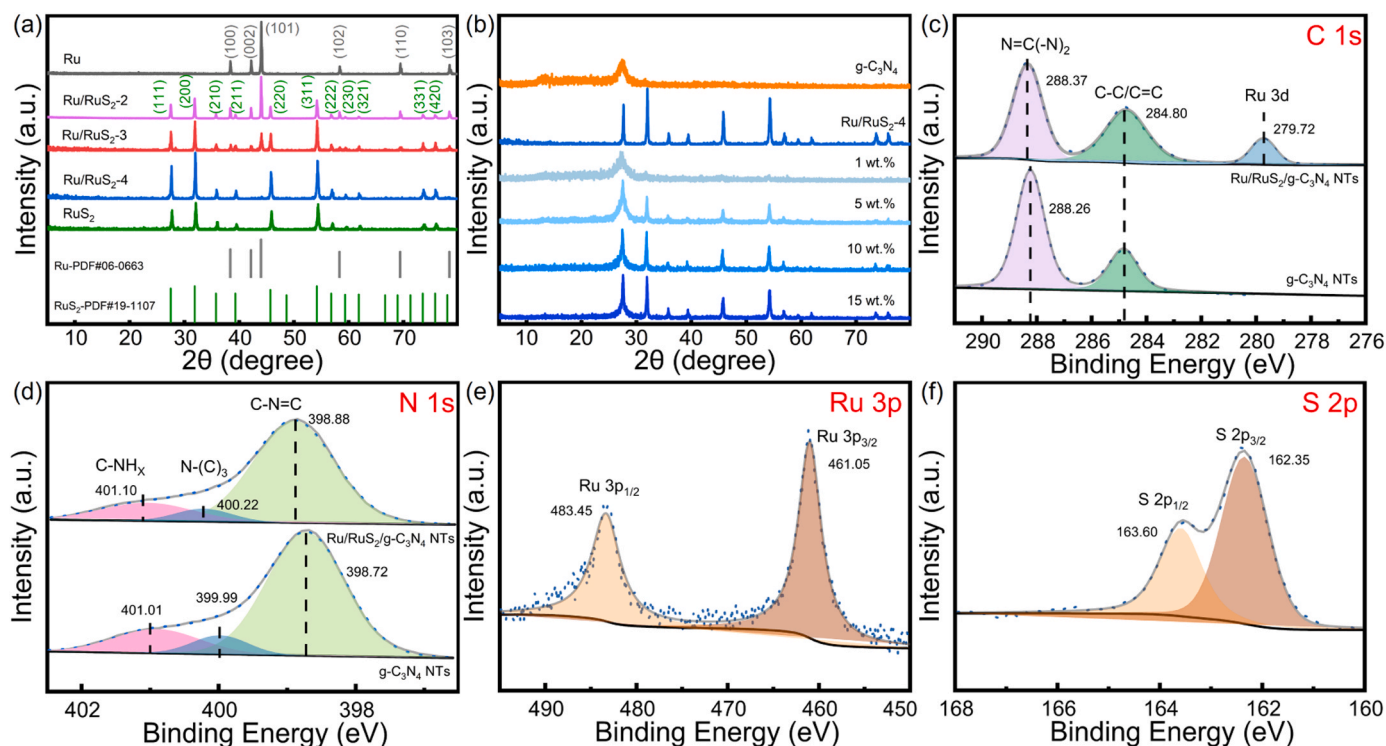
Scheme 1. Schematic diagram of the preparation of g-C$_3$N$_4$ NTs.

Scheme 2. Schematic diagram of the preparation of Ru/RuS$_2$.

Scheme 3. Schematic diagram of the preparation of Ru/RuS$_2$/g-C$_3$N$_4$ NTs.

Fig. 1. XRD patterns of (a) Ru/RuS$_2$ with different RuCl$_3$/K$_2$S ratios (n_{RuCl3}:n_{K2S} = 1:1, 1:2, 1:3, 1:4 and 1:5) and (b) g-C$_3$N$_4$ NTs, Ru/RuS$_2$-4 and Ru/RuS$_2$/g-C$_3$N$_4$ NTs (containing 1, 5, 10 and 15 wt% of Ru/RuS$_2$, respectively); (c) C 1 s, (d) N 1 s, (e) Ru 3p and (f) S 2p core-level XPS spectra of 10 wt% Ru/RuS$_2$/g-C$_3$N$_4$ NTs.

transfer at the interface of Ru/RuS$_2$ and g-C$_3$N$_4$ NTs is beneficial to optimizing charge distribution, thus improving photocatalytic performance. Meanwhile, the Ru 3d XPS spectrum of 10 wt% Ru/RuS$_2$/g-C$_3$N$_4$ NTs shows the binding energy at 279.72 eV, attributed to Ru^{4+} 3d$_{5/2}$ as shown in Fig. 1c. For Ru 3p XPS spectrum in Fig. 1e, the peaks with binding energies located at 461.05 and 483.45 eV correspond to Ru 3p$_{3/2}$ and Ru 3p$_{1/2}$, respectively [70]. The S 2p XPS spectrum shows the characteristic peaks at 162.35 and 163.60 eV, attributing to S 2p$_{3/2}$ and S 2p$_{1/2}$, respectively (Fig. 1f) [64]. The synergistic effect of Ru/RuS$_2$ as dual co-catalysts shows strong electronic synergistic interaction between the interfaces, improves the electron distribution and facilitates the effective transfer of charges from g-C$_3$N$_4$ to the cocatalyst surface, thus enhancing the catalytic performance. The above XPS spectra analysis shows the Ru/RuS$_2$/g-C$_3$N$_4$ NTs were successfully synthesized by loading Ru/RuS$_2$ on g-C$_3$N$_4$ NTs.

To further confirm the successful loading of Ru/RuS$_2$ on g-C$_3$N$_4$ NTs, the morphology and structure of 10 wt% Ru/RuS$_2$/g-C$_3$N$_4$ NTs were observed by scanning electron microscopy (SEM) and transmission electron microscopy (TEM) with energy dispersive spectrometer (EDS), as shown in Fig. 2. The Ru/RuS$_2$ heterostructure obtained by the molten salt method using RuCl$_3$ and K$_2$S as raw materials has a nanoparticle-like morphology with a diameter of about 60–80 nm (Fig. 2a). The g-C$_3$N$_4$ NTs synthesized via hydrothermal and heat treatment shows hexagonal columnar shape with nanosheets stacked and diameter of 2–4 μm (Fig. 2b). The mesoporous structure with lamellar channels could increase the specific surface area, supply active sites for surface reaction, promote charge and mass transfer. The morphology and structure of Ru/RuS$_2$/g-C$_3$N$_4$ NTs in Fig. 2c and d also show a 3D mesoporous structure with interlayer channels from 2D nanosheet stacks, which could help to create space potential difference between the layers, and be beneficial
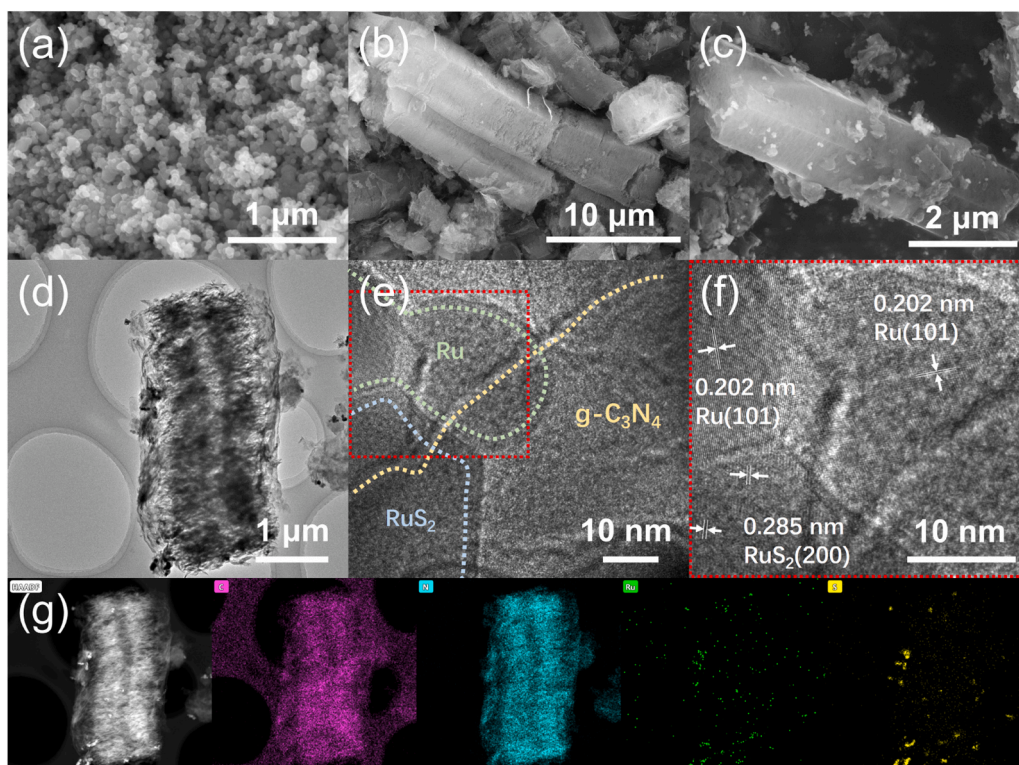
Fig. 2. SEM images of (a) Ru/RuS$_2$ and (b) g-C$_3$N$_4$ NTs; (c) SEM, (d-f) TEM and (g) EDS elemental mappings of Ru/RuS$_2$/g-C$_3$N$_4$ NTs.
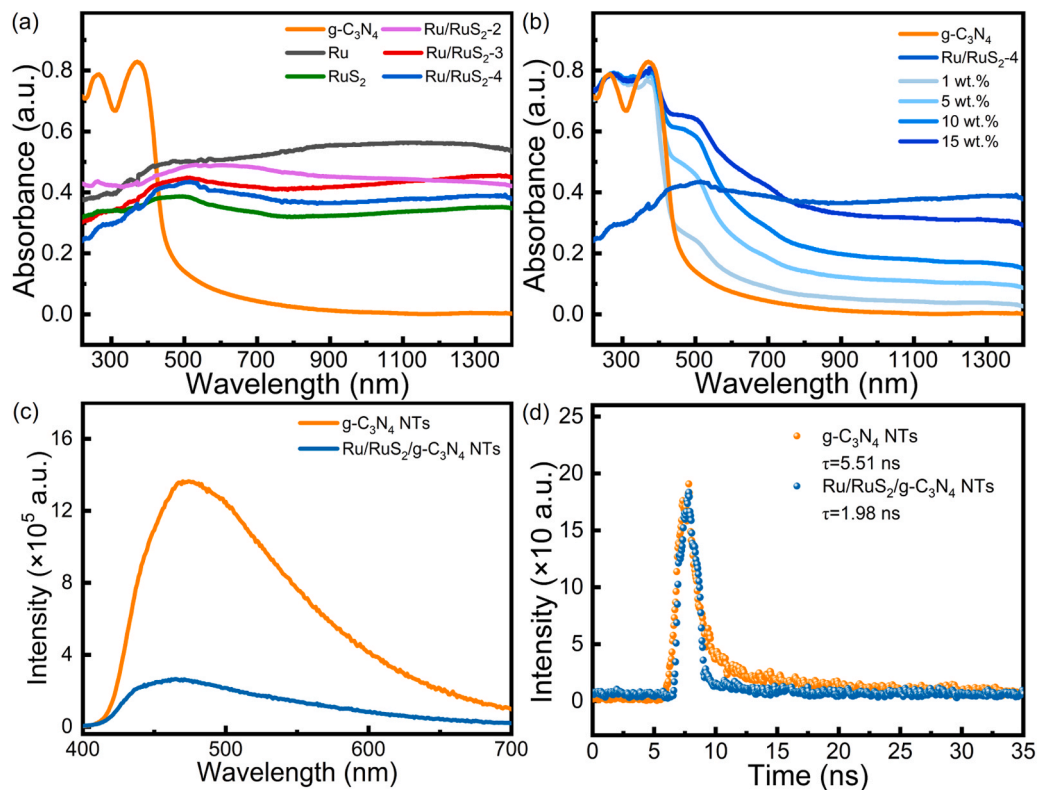

Fig. 3. UV-Vis DRS of (a) g-C$_3$N$_4$ NTs and Ru/RuS$_2$ with different RuCl$_3$/K$_2$S ratios (n$_{RuCl3}$:n$_{K2S}$ = 1:1, 1:2, 1:3, 1:4 and 1:5); UV-Vis DRS of (b) g-C$_3$N$_4$ NTs, Ru/RuS$_2$-4 and Ru/RuS$_2$/g-C$_3$N$_4$ NTs (containing 1, 5, 10 and 15 wt% of Ru/RuS$_2$, respectively); (c) Steady and (d) time-resolved PL spectra of g-C$_3$N$_4$ NTs and 10 wt% Ru/RuS$_2$/g-C$_3$N$_4$ NTs.

for migration of electrons and mass, and the occurrence of surface reactions [71].

The heterogeneous interface of Ru/RuS$_2$ as dual co-catalysts was shown through high-resolution TEM images (Fig. 2e and f). In the upper right corner of Fig. 2f, Ru atoms are arranged in a hexagonal close-packed (hcp) structure and the lattice spacing of 0.202 nm can be indexed to the (101) crystal face of Ru [66], which is consistent with the XRD results. In addition, clear lattice stripes of 0.285 nm could be observed at the bottom, corresponding to the (200) crystal plane of RuS$_2$ [64]. Therefore, Ru/RuS$_2$ heterointerfaces as dual co-catalysts can be formed between overlapping regions in Fig. 2e. High-angle annular dark-field scanning transmission electron microscopy (HAADF-STEM) images and their associated EDS elemental mapping images of Ru/RuS$_2$/g-C$_3$N$_4$ NTs also shows the uniform distribution of C and N, and the presence of Ru and S in Fig. 2g, indicating that the Ru/RuS$_2$ heterostructure was successfully constructed and the Ru/RuS$_2$ as dual co-catalysts are loaded on the surface of g-C$_3$N$_4$ NTs, thus proving the successful synthesis of Ru/RuS$_2$/g-C$_3$N$_4$ NTs.

UV-Vis Diffuse Reflection Spectroscopy (DRS) was performed to characterize light absorption properties of g-C$_3$N$_4$ NTs, Ru/RuS$_2$ with different RuCl$_3$/K$_2$S ratios (n_{RuCl3}:n_{K2S} = 1:1, 1:2, 1:3, 1:4 and 1:5) and Ru/RuS$_2$/g-C$_3$N$_4$ NTs (containing 1, 5, 10 and 15 wt% of Ru/RuS$_2$, respectively), as shown in Fig. 3a and b. As shown in Fig. 3a, RuS$_2$ (green curve) exhibits visible light absorption characteristics from 250 nm to 800 nm, and metallic phase Ru with gray curve shows near-infrared light absorption characteristics from 800 nm to 1400 nm. The Ru/RuS$_2$ heterostructure as dual co-catalysts show enhanced near-infrared light absorption intensity from metallic phase Ru and reduced visible light absorption intensity of RuS$_2$ as the proportion of Ru increases. The light absorption characteristics of the cocatalyst in the visible and near-infrared regions allow carriers to be excited with lower energy, which will provide the catalyst with higher photogenerated carrier concentration, thus enhancing the photocatalytic performance.

The light absorption properties of Ru/RuS$_2$/g-C$_3$N$_4$ NTs composite photocatalysts with different weight ratios of Ru/RuS$_2$ were studied to further explore the role of cocatalyst in Fig. 3b. The intensity and range of light absorption of Ru/RuS$_2$/g-C$_3$N$_4$ NTs are significantly enhanced after the loading of Ru/RuS$_2$. The absorption edge of g-C$_3$N$_4$ NT is 455 nm, and the absorption edge of Ru/RuS$_2$/g-C$_3$N$_4$ NTs expands to the near-infrared region as the loading amount of Ru/RuS$_2$ increases from 1 to 15 wt%, indicating that Ru/RuS$_2$ as dual co-catalysts loaded on the surface of g-C$_3$N$_4$ NTs increases the range and intensity of light absorption, thereby improves the generation of photogenerated carriers. However, too much cocatalyst loaded on g-C$_3$N$_4$ NTs may lead to a shadow effect, thereby affecting the photocatalytic performance of Ru/RuS$_2$/g-C$_3$N$_4$ NTs, which was proven in the photocatalytic hydrogen evolution test. Meanwhile, the band gap energy (Eg) of g-C$_3$N$_4$ NTs is calculated to be approximately 2.73 eV through the formula of $(\alpha h\nu)1/2 \propto h\nu - E_g$ in Fig. S2. The steady photoluminescence (PL) tests of g-C$_3$N$_4$ NTs and Ru/RuS$_2$/g-C$_3$N$_4$ NTs were performed to explore the important role of Ru/RuS$_2$ as dual co-catalysts loaded on g-C$_3$N$_4$ NTs (Fig. 3c). The Ru/RuS$_2$/g-C$_3$N$_4$ NTs shows significant decrease than g-C$_3$N$_4$ NTs in steady PL spectra as the unique structure of g-C$_3$N$_4$ NTs and Ru/RuS$_2$ as dual co-catalysts could improve the excitation and transfer process of carriers, thus suppress the recombination of electrons and holes [72–74]. The time-resolved photoluminescence (TRPL) tests of g-C$_3$N$_4$ NTs and Ru/RuS$_2$/g-C$_3$N$_4$ NTs were performed at the emission wavelength of the sample to explore the important role in carrier dynamics (Fig. 3d). The results show that the loading of Ru/RuS$_2$ as dual co-catalysts gradually shortens the PL life. The dual co-catalyst sites provide electron trapping states to accept photoexcited electrons and suppress carrier recombination [72]. The photogenerated electrons are transferred from the catalyst to the cocatalyst and participate in the hydrogen evolution reaction, thereby improving the photocatalytic activity [73,74]. Based on the optical properties, the presence of Ru/RuS$_2$ as dual co-catalysts effectively suppresses carrier recombination and

provides more efficient carrier separation and transfer.

To determine the influence of the unique structure of g-C$_3$N$_4$ NTs, and Ru/RuS$_2$ as dual co-catalysts on the photocatalytic activity of g-C$_3$N$_4$, the transient photocurrent (TPC), electrochemical impedance spectroscopy (EIS) and linear sweep voltammetry (LSV) tests of g-C$_3$N$_4$ NTs and Ru/RuS$_2$/g-C$_3$N$_4$ NTs were systematically studied using a typical three-electrode electrochemical system in 0.5 mol/L Na$_2$SO$_4$ (Fig. 4). In Fig. 4a, g-C$_3$N$_4$ NTs, Ru/g-C$_3$N$_4$ NTs and RuS$_2$/g-C$_3$N$_4$ NTs process the lowest transient photocurrent response. However, the Ru/RuS$_2$/g-C$_3$N$_4$ NTs with Ru/RuS$_2$ heterostructure as dual co-catalysts show enhanced transient photocurrent response, and Ru/RuS$_2$-4 shows especially the best performance, which proves that the Ru/RuS$_2$ dual co-catalysts with a lower Ru:S ratio can enhance light absorption and generate more photoexcited carriers for photocatalytic reactions. Generally, the smaller radius of curvature in EIS corresponds to the smaller charge transfer resistance. As shown in Fig. 4b, the Ru/RuS$_2$/g-C$_3$N$_4$ NTs with Ru/RuS$_2$ heterostructure as dual co-catalysts show smaller charge transfer resistance than g-C$_3$N$_4$ NTs, Ru/g-C$_3$N$_4$ NTs and RuS$_2$/g-C$_3$N$_4$ NTs under AM-1.5 irradiation. The unique structure of g-C$_3$N$_4$ NTs and Ru/RuS$_2$ as dual co-catalysts could decrease the electrons migration resistance, thus promoting the carrier transfer from g-C$_3$N$_4$ NTs to Ru/RuS$_2$ dual co-catalysts and participate in the photocatalytic reaction. Meanwhile, the Ru/RuS$_2$/g-C$_3$N$_4$ NTs with Ru/RuS$_2$ heterostructure as dual co-catalysts also show a lower overpotential at the same current density in the LSV curve in Fig. 4c, corresponding to the stronger catalytic ability. Surface photovoltage (SPV) spectroscopy was performed on g-C$_3$N$_4$ NTs and Ru/RuS$_2$/g-C$_3$N$_4$ NTs to further explore the photogenerated carrier separation efficiency (Fig. 4d). The SPV signals of Ru/RuS$_2$/g-C$_3$N$_4$ NTs, like the DRS in Fig. 3b, both show the decrease at 350 nm and enhancement from 450 to 800 nm, indicating that the loading of Ru/RuS$_2$ as dual co-catalysts on g-C$_3$N$_4$ NTs enhancing the light absorption and charge transfer, thus improving the photocatalytic activity. Besides, the Ru/RuS$_2$/g-C$_3$N$_4$ NTs shows the stronger SPV signal compared with g-C$_3$N$_4$ NTs, due that the loading of Ru/RuS$_2$ as dual co-catalysts on g-C$_3$N$_4$ NTs enhances the strong interfacial interaction of Ru/RuS$_2$/g-C$_3$N$_4$ NTs, thus improves the capture ability of photogenerated electrons and reduces the recombination rate of photogenerated carriers, thereby improving the utilization rate of photogenerated electrons and enhancing the photocatalytic performance [75,76]. The above photoelectrochemical tests show that Ru/RuS$_2$ as dual co-catalysts is loaded on the surface of the g-C$_3$N$_4$ NTs with lamellar hexagonal prism, which could generate more photoexcited carriers, and reduce electrochemical impedance to promote carrier transport to surface active sites, thus facilitating surface chemical reactions.

Photocatalytic hydrogen evolution tests of g-C$_3$N$_4$, g-C$_3$N$_4$ NTs and Ru/RuS$_2$/g-C$_3$N$_4$ NTs with different weight ratios, cocatalysts and sacrificial reagents under 300 W Xe lamp with AM-1.5 filter were carried out to test the photocatalytic activity (Fig. 5). g-C$_3$N$_4$ and g-C$_3$N$_4$ NTs show lower hydrogen evolution activity as the rapid recombination of carriers in Fig. 5a and b, corresponding to the lower activity in the optics and photoelectrochemistry characterization tests (Figs. 3 and 4). The hydrogen evolution activity of Ru/RuS$_2$/g-C$_3$N$_4$ NTs after the loading of Ru/RuS$_2$ as dual co-catalysts was enhanced with the loading of Ru/RuS$_2$ from 1 wt% to 10 wt% (Fig. 5a), as the unique structure of g-C$_3$N$_4$ NTs, and Ru/RuS$_2$ as dual co-catalysts could generate more photoexcited carriers, and reduce electrochemical impedance to promote carrier transport to surface active sites, thus facilitating surface chemical reactions. But the activity of Ru/RuS$_2$/g-C$_3$N$_4$ NTs decreased as the Ru/RuS$_2$ increased from 10 wt% to 15 wt% for the overdose of Ru/RuS$_2$ on Ru/RuS$_2$/g-C$_3$N$_4$ NTs led to the shield effect and suppressed the light absorption, thus decreased the generation of photocarriers. Meanwhile, the hydrogen evolution activity of 10 wt% Ru/RuS$_2$/g-C$_3$N$_4$ NTs with different RuCl$_3$/K$_2$S ratios (n_{RuCl3}:n_{K2S} = 1:1, 1:2, 1:3, 1:4 and 1:5) were tested in Fig. 5b, and 10 wt% Ru/RuS$_2$/g-C$_3$N$_4$ NTs with RuCl$_3$/K$_2$S ratios of 1:4 displayed the highest hydrogen evolution activity as shown
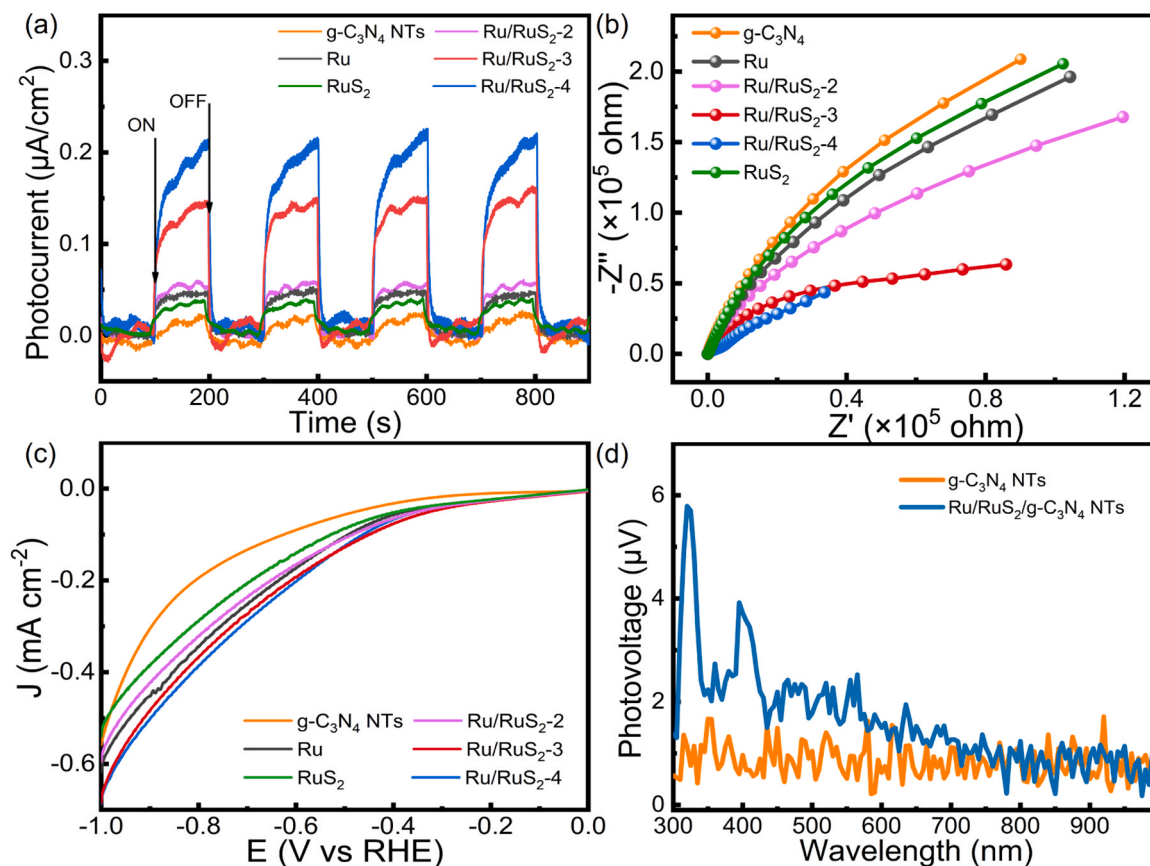
Fig. 4. (a) TPC, (b) EIS and (c) LSV curves of g-C$_3$N$_4$ NTs and Ru/RuS$_2$/g-C$_3$N$_4$ NTs with different RuCl$_3$/K$_2$S ratios (n$_{RuCl3}$:n$_{K2S}$ = 1:1, 1:2, 1:3, 1:4 and 1:5); (d) SPV spectra of g-C$_3$N$_4$ NTs and 10 wt% Ru/RuS$_2$/g-C$_3$N$_4$ NTs.
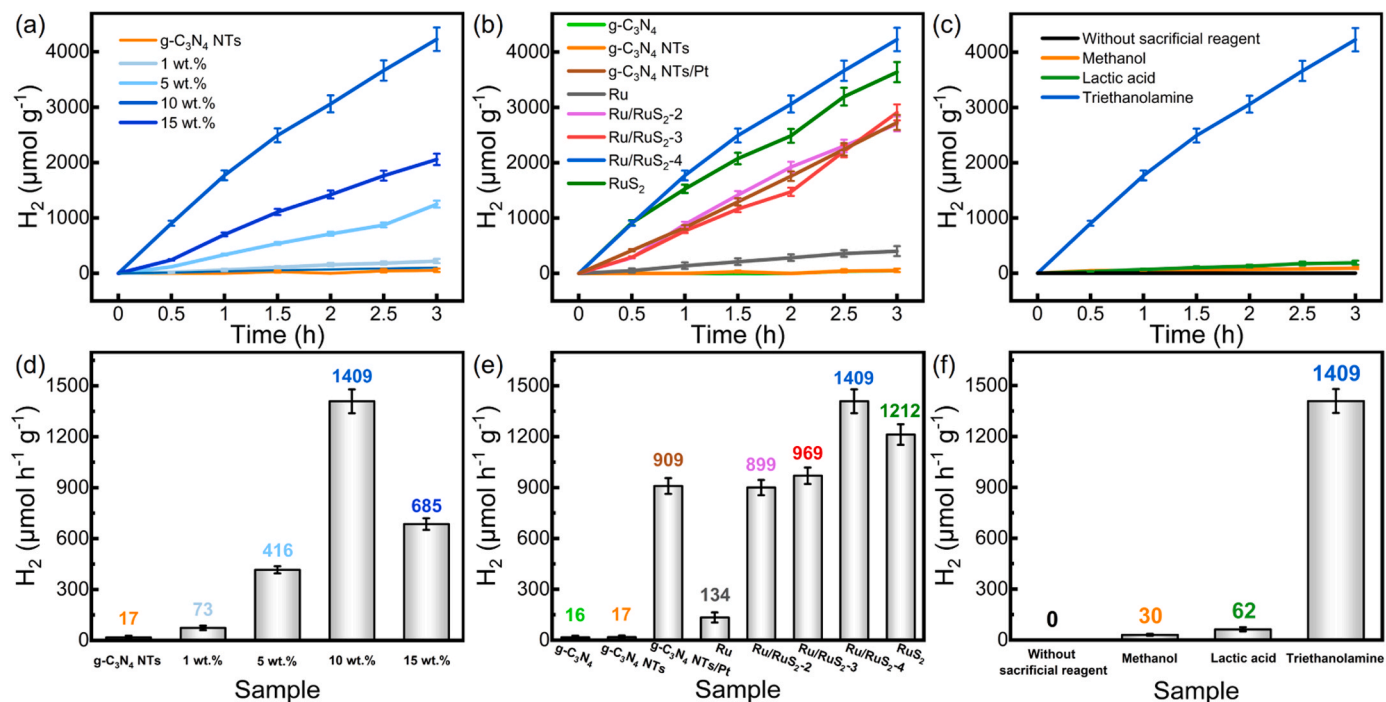

Fig. 5. Photocatalytic hydrogen evolution activity and rate of (a, d) g-C$_3$N$_4$ NTs and Ru/RuS$_2$/g-C$_3$N$_4$ NTs (containing 1, 5, 10 and 15 wt% of Ru/RuS$_2$, respectively); (b, e) g-C$_3$N$_4$, g-C$_3$N$_4$ NTs, g-C$_3$N$_4$ NTs/Pt and Ru/RuS$_2$/g-C$_3$N$_4$ NTs with different RuCl$_3$/K$_2$S ratios (n$_{RuCl3}$:n$_{K2S}$ = 1:1, 1:2, 1:3, 1:4 and 1:5); (c, f) Ru/RuS$_2$/g-C$_3$N$_4$ NTs with different sacrificial reagent under AM-1.5 irradiation.

in Fig. 5d and e. In addition, the effects of different sacrificial reagents on the photocatalytic hydrogen evolution of Ru/RuS$_2$/g-C$_3$N$_4$ NTs were compared. Fig. 5c and f show that Ru/RuS$_2$/g-C$_3$N$_4$ NTs with triethanolamine (TEOA) as the sacrificial reagent possess the best photocatalytic performance for the g-C$_3$N$_4$ NTs prefer to produce hydrogen in the weakly alkaline environment provided by TEOA.

The Ru/RuS$_2$/g-C$_3$N$_4$ NTs showed enhanced photocatalytic hydrogen production rate (1409 μmol·g^{-1}·h^{-1}), 1.16 times of the RuS$_2$/g-C$_3$N$_4$ NTs (1212 μmol·g^{-1}·h^{-1}), 10.51 times of Ru/g-C$_3$N$_4$ NTs (134 μmol·g^{-1}·h^{-1}), 1.55 times of Pt/g-C$_3$N$_4$ NTs (909 μmol·g^{-1}·h^{-1}), and 82.88 times of the pure g-C$_3$N$_4$ NTs (17 μmol·g^{-1}·h^{-1}). Meanwhile, the hydrogen evolution activity of Ru/RuS$_2$/g-C$_3$N$_4$ NTs kept stability after 18 h reaction (Fig. S3). The AQE of 20 mg Ru/RuS$_2$/g-C$_3$N$_4$ NTs is 3.92% at 370 nm. The improved photocatalytic performance of Ru/RuS$_2$/g-C$_3$N$_4$ NTs is attributed to that the g-C$_3$N$_4$ NTs with hexagonal porous morphology have the porous sheet-like internal structure, which is beneficial to increase the specific surface area, thereby increasing light absorption and facilitating electron and mass transport. The loading of Ru/RuS$_2$ as dual co-catalysts in the g-C$_3$N$_4$ NTs can extend the range of light absorption to visible light and near-infrared light regions, respectively, and provide the heterointerfaces as surface active sites to capture carriers to participate in the surface hydrogen evolution reaction. The Ru/RuS$_2$ heterointerfaces as dual co-catalysts are self-assembled on the surface of g-C$_3$N$_4$ NTs, which exhibits higher photogenerated carrier

Table 1
Comparison of hydrogen evolution rate between Ru/RuS$_2$/g-C$_3$N$_4$ NTs and other photocatalysts.

Catalyst	Test conditions	Light source	H$_2$ evolution (μmol g^{-1} h^{-1})	Ref.
Ru/g-C$_3$N$_4$ nanosheets	10 vol% TEOA aqueous solution	300 W Xe arc lamp with 400 nm cutoff optical filter	1070.0	[77]
Ru/MXene/ TiO$_2$	10 vol% methanol aqueous solution	300 W Xe arc lamp with cutoff optical filter from 350 to 780 nm	235.3	[78]
Au/g-C$_3$N$_4$ nanosheets	20 vol% methanol aqueous solution	300 W Xe arc lamp	265.0	[79]
Au/P-g-C$_3$N$_4$ nanosheets	20 vol% methanol aqueous solution	300 W Xe arc lamp	485.0	[79]
Pt/bulk g-C$_3$N$_4$	10 vol% TEOA aqueous solution	350 W Xe arc lamp	760.0	[80]
Pt/t-ZrO$_2$/g-C$_3$N$_4$ nanosheets	10 vol% TEOA aqueous solution	300 W Xe arc lamp with 420 nm cutoff optical filter	722.5	[81]
Benzene-ring grafted g-C$_3$N$_4$ nanotubes	10 vol% TEOA aqueous solution	300 W Xe arc lamp with 420 nm cutoff optical filter	666.0	[82]
7 wt% CoO/g-C$_3$N$_4$ nanotubes	10 vol% TEOA aqueous solution	300 W Xe arc lamp with 420 nm cutoff optical filter	788.6	[83]
2 wt% Pt/g-C$_3$N$_4$ nanotubes	10 vol% TEOA aqueous solution	300 W Xe arc lamp with 420 nm cutoff optical filter	135.0	[84]
Ru/RuS$_2$/g-C$_3$N$_4$ NTs	20 vol% TEOA aqueous solution	300 W Xe arc lamp with Am-1.5 filter	1409	Our work

concentration and lower charge migration resistance than RuS$_2$ and Ru, showing the synergistic effect to facilitate the generation and migration of carriers and provides active sites for surface reactions, therefore improving photocatalytic hydrogen evolution.

The related Ru-based and g-C$_3$N$_4$-based photocatalysts were listed (Table 1) to compare the photocatalytic activity of Ru/RuS$_2$/g-C$_3$N$_4$ NTs. The Ru/RuS$_2$/g-C$_3$N$_4$ NTs show better photocatalytic performance than other photocatalysts, showing the important role of unique morphology of g-C$_3$N$_4$ NTs, and Ru/RuS$_2$ as dual co-catalysts for improving the photocatalytic hydrogen evolution.

The density functional theory (DFT) calculation further revealed the mechanism of enhanced hydrogen evolution reaction activity of Ru/RuS$_2$/g-C$_3$N$_4$. The top and front views of the hydrogen adsorption model used to describe g-C$_3$N$_4$, Ru/g-C$_3$N$_4$, RuS$_2$/g-C$_3$N$_4$, RuS$_2$/Ru/g-C$_3$N$_4$ and Ru/RuS$_2$/g-C$_3$N$_4$ and their calculated H binding free energies (ΔG_{H^*}) in HER were displayed in Fig. 6. The unsaturated N and C$_1$, C$_2$ of g-C$_3$N$_4$ were assumed to be the photocatalytic active sites for HER in Fig. 6a. And the surface exposed Ru and/or S atoms of Ru/g-C$_3$N$_4$, RuS$_2$/g-C$_3$N$_4$, RuS$_2$/Ru/g-C$_3$N$_4$ and Ru/RuS$_2$/g-C$_3$N$_4$ were assumed to be the photocatalytic active sites for HER in Fig. 6b-e. The ΔG_{H^*} of those photocatalytic active sites are shown in Fig. 6f. The ideal ΔG_{H^*} of photocatalytic active sites for HER is 0 eV. The ΔG_{H^*} for unsaturated N and C$_1$ of g-C$_3$N$_4$ were − 2.64 and − 0.88 eV, which was far from 0 eV for HER potential and unfavorable for H desorption (Fig. 6a and f). The ΔG_{H^*} of C$_2$ of g-C$_3$N$_4$ was − 0.46 eV, which was beneficial to the desorption of H, but the rapid carrier recombination of g-C$_3$N$_4$ suppressed its photocatalytic performance. As shown in Fig. 6b and f, the ΔG_{H^*} for Ru$_1$ and Ru$_2$ sites of Ru/g-C$_3$N$_4$ with (101) crystal face of Ru are − 0.70 and − 0.84 eV. The more negative ΔG_{H^*} in kinetics was conducive to the selective adsorption of H, but H needed to overcome more energy to desorb from the Ru site from the thermodynamic perspective, thus inhibiting HRE activity, which was consistent with the reports in the relevant literature in the introduction part [50,52,57,58]. The ΔG_{H^*} for Ru sites of RuS$_2$/g-C$_3$N$_4$ with (200) crystal face of RuS$_2$ was − 0.66 eV in Fig. 6c and f, which was also far from 0 eV for HER potential and unfavorable for H desorption, corresponding to general HER activity [59–62]. The ΔG_{H^*} for S sites of RuS$_2$/g-C$_3$N$_4$ and RuS$_2$/-Ru/g-C$_3$N$_4$ were 0.33 and 0.28 eV in Fig. 6c, d and f, however, H tends to be selectively adsorbed on the Ru sites of these two structures from the kinetic perspective as the Ru sites possessed more negative ΔG_{H^*}. The ΔG_{H^*} of Ru sites (−1.43 eV) on RuS$_2$/Ru/g-C$_3$N$_4$ was more negative than Ru sites (−0.66 eV) on RuS$_2$/g-C$_3$N$_4$ for the HER activity, indicating that the participation of Ru in the formation of the heterointerface formed strong electronic interaction and provides more charge energy at the Ru sites on RuS$_2$/Ru/g-C$_3$N$_4$ for the dissociation of H-OH (Fig. 6d and f) [50]. And the Ru$_1$ sites (−0.40 eV) on Ru/RuS$_2$/g-C$_3$N$_4$ were more active than Ru sites on Ru/g-C$_3$N$_4$ (−0.70 and −0.84 eV), RuS$_2$/g-C$_3$N$_4$ (−0.66 eV), RuS$_2$/Ru/g-C$_3$N$_4$ (−1.43 eV) and Ru/RuS$_2$/g-C$_3$N$_4$ (−0.88 eV) for the HER activity as it possessed smaller hydrogen desorption energy and was thermodynamically favorable with the smallest ΔG_{H^*} (Fig. 6e and f). These results displayed that Ru/RuS$_2$ heterointerface structure as a double cocatalyst supported on g-C$_3$N$_4$ could form strong electron cooperative interaction and promote charge transfer, thus reducing ΔG_{H^*} of RuS$_2$ and desorption energy of Ru, synergistically promoting the selectivity and activity of HER kinetically and thermodynamically respectively, finally promoting the photocatalytic hydrogen evolution activity.

Besides, the E$_{CB}$ of g-C$_3$N$_4$ NTs was tested by Mott-Schottky (Fig. S4). The flat band potential (E$_{FB}$) of g-C$_3$N$_4$ NTs was about − 1.19 V vs. Ag/AgCl, corresponding to − 0.99 V vs. NHE. Generally, the E$_{CB}$ value of the n-type semiconductor was lower than E$_{FB}$ by ~ 0.1 V, therefore the E$_{CB}$ of g-C$_3$N$_4$ NTs was about − 1.09 V vs. NHE. Combining the band structure test in the experiment, the band structure of Ru/RuS$_2$/g-C$_3$N$_4$ NTs was shown in Scheme 4.

Based on the above analysis, the photocatalytic mechanism of Ru/RuS$_2$/g-C$_3$N$_4$ NTs was shown in Scheme 4. Firstly, photoexcited carriers

Fig. 6. Top and front views of the hydrogen adsorption model used to describe (a) g-C_3N_4, (b) Ru/g-C_3N_4, (c) RuS_2/g-C_3N_4, (d) RuS_2/Ru/g-C_3N_4 and (e) Ru/RuS_2/g-C_3N_4, and the colors of elements are: white for H, gray for C, blue for N, green for Ru and yellow for S atom; (f) The calculated ΔG_{H*} of the above models in HER.

in Ru/RuS_2/g-C_3N_4 NTs are generated under light illumination, and the electrons subsequently transfer from the valence band (VB) to the conduction band (CB). Then, the electrons are captured by the Ru/RuS_2 dual co-catalysts on g-C_3N_4 NTs to take part in the reduction reaction to evolute H_2. The electrons prefer to transfer to the thermodynamically favorable Ru/RuS_2 dual co-catalysts in Ru/RuS_2/g-C_3N_4 NTs, which suppresses the recombination of electrons and holes, and improve the photocatalytic performance of Ru/RuS_2/g-C_3N_4 NTs. The holes move to the g-C_3N_4 NTs surface due to electron migration, and react with TEOA to form oxidation products. The Ru/RuS_2/g-C_3N_4 NTs show advantages as follows: The g-C_3N_4 NTs with hexagonal porous morphology have a porous sheet-like internal structure, which is beneficial to increase the specific surface area, thereby increasing light absorption and facilitating electron and mass transport. The loading of Ru/RuS_2 as dual co-catalysts in the g-C_3N_4 NTs can extend the range of light absorption to visible light and near-infrared light regions, respectively, and provide the heterointerfaces as surface active sites to capture carriers to participate in the surface hydrogen evolution reaction. The Ru/RuS_2 heterointerfaces as

dual co-catalysts are self-assembled on the surface of g-C_3N_4 NTs and show strong electronic synergistic interaction between the interfaces, reduces ΔG_{H*} of RuS_2 and desorption energy of Ru, and promotes the selectivity and activity of HER kinetically and thermodynamically respectively, which exhibits higher photogenerated carrier concentration and lower charge migration resistance than RuS_2 and Ru, showing the synergistic effect to facilitate the generation and migration of carriers and provides active sites for surface reactions, therefore improving photocatalytic hydrogen evolution.

4. Conclusions

To sum up, the Ru/RuS_2 nanoparticles as dual co-catalysts were self-assembled on the surface of g-C_3N_4 nanotubes (Ru/RuS_2/g-C_3N_4 NTs) for photocatalytic H_2 production. The Ru/RuS_2/g-C_3N_4 NTs showed greatly enhanced photocatalytic H_2 production activity (1409 μmol·g^{-1}·h^{-1}), 1.16 times of the RuS_2/g-C_3N_4 NTs (1212 μmol·h^{-1}·g^{-1}), 10.51 times of Ru/g-C_3N_4 NTs (134 μmol·g^{-1}·h^{-1}), and 82.88 times of

Scheme 4. Schematic of the photocatalytic mechanism of Ru/RuS$_2$/g-C$_3$N$_4$ NTs.

the pure g-C$_3$N$_4$ NTs (17 μmol·g^{-1}·h^{-1}). Besides, the apparent quantum yield value (AQE) of 20 mg Ru/RuS$_2$/g-C$_3$N$_4$ NTs is 3.92% at 370 nm. The characterization and DFT analysis have proven the benefits of Ru/RuS$_2$/g-C$_3$N$_4$ NTs are shown as follows: 1) The g-C$_3$N$_4$ NTs with hexagonal porous morphology have the porous sheet-like internal structure, which is beneficial to increase the specific surface area, thereby increasing light absorption and facilitating electron and mass transport. 2) The loading of Ru/RuS$_2$ as dual co-catalysts in the g-C$_3$N$_4$ NTs can extend the range of light absorption to visible light and near-infrared light regions, respectively, and provide the heterointerfaces as surface active sites to capture carriers to take part in the surface H$_2$ evolution reaction. 3) The Ru/RuS$_2$ heterointerfaces as dual co-catalysts are self-assembled on the surface of g-C$_3$N$_4$ NTs and show strong electronic synergistic interaction between the interfaces, reducing ΔG_{H*} of RuS$_2$ and desorption energy of Ru, and promoting the selectivity and activity of HER kinetically and thermodynamically respectively, which exhibits higher photogenerated carrier concentration and lower charge migration resistance than RuS$_2$ and Ru, showing the synergistic effect to facilitate the generation and migration of carriers and provides active sites for surface reactions, therefore improving photocatalytic hydrogen evolution.

CRediT authorship contribution statement

Wang Xinyu: Writing – original draft. **Zhang Hangzhou:** Writing – review & editing. **Xue Yanjun:** Data curation. **Ren Jiali:** Methodology. **You Junhua:** Writing – review & editing. **Tian Jian:** Writing – review & editing.

Declaration of Competing Interest

The authors declare that they have no known competing financial interests or personal relationships that could have appeared to influence the work reported in this paper.

Data availability

Data will be made available on request.

Acknowledgment

Appendix A. Supporting information

Supplementary data associated with this article can be found in the online version at doi:10.1016/j.apcatb.2024.123722.

References

[1] M. Zhou, X. Li, Influence of green finance and renewable energy resources over the sustainable development goal of clean energy in China, Resour. Policy 78 (2022) 102816.

[2] J. You, J. Li, Z. Wang, M. Baghayeri, H. Zhang, Application of Co$_3$O$_4$ nanocrystal/rGO for simultaneous electrochemical detection of cadmium and lead in environmental waters, Chemosphere 335 (2023) 139133.

[3] Y. Zhao, J. You, L. Wang, W. Bao, R. Yao, Recent advances in Ni$_3$S$_2$-based electrocatalysts for oxygen evolution reaction, Int. J. Hydrog. Energy 46 (2021) 39146–39182.

[4] D. Animashaun, M. Hussain, Automated micro-crack detection within photovoltaic manufacturing facility via ground modelling for a regularized convolutional network, Sensors 23 (2023) 6235.

[5] S. Vázquez-Aveledo, R.J. Romero, M. Montiel-González, J. Cerezo, Control strategy based on artificial intelligence for a double-stage absorption heat transformer, Processes 11 (2023) 1632.

[6] F. Almomani, A. Al-Rababah, M. Tawalbeh, A. Al-Othman, A comprehensive review of hydrogen generation by water splitting using 2D nanomaterials: Photo vs electro-catalysis, Fuel 332 (2023) 125905.

[7] Z. Li, J. Liu, J. Zhao, R. Shi, G.I. Waterhouse, X.D. Wen, T. Zhang, Photo-driven hydrogen production from methanol and water using plasmonic Cu nanoparticles derived from layered double hydroxides, Adv. Funct. Mater. 33 (2023) 2213672.

[8] A. Fujishima, K. Honda, Electrochemical photolysis of water at a semiconductor electrode, Nature 238 (1972) 37–38.

[9] T. Li, N. Tsubaki, Z. Jin, S-scheme heterojunction in photocatalytic hydrogen production, J. Mater. Sci. Technol. 169 (2024) 82–104.

[10] M. Tayyab, Y. Liu, Z. Liu, Z. Xu, W. Yue, L. Zhou, J. Lei, J. Zhang, A new breakthrough in photocatalytic hydrogen evolution by amorphous and chalcogenide enriched cocatalysts, Chem. Eng. J. 455 (2023) 140601.

[11] X. Wang, J. Gong, Y. Dong, S. An, X. Zhang, J. Tian, Energy band engineering of hydroxyethyl group grafted on the edge of 3D g-C$_3$N$_4$ nanotubes for enhanced photocatalytic H$_2$ production, Mater. Today Phys. 27 (2022) 100806.

[12] S. Liang, G. Sui, D. Guo, Z. Luo, R. Xu, H. Yao, J. Li, C. Wang, g-C$_3$N$_4$-wrapped nickel doped zinc oxide/carbon core-double shell microspheres for high-performance photocatalytic hydrogen production, J. Colloid Interface Sci. 635 (2023) 83–93.

[13] C. Dai, Z. Feng, Q. Hu, J. Qiu, J. You, R. Guo, H. Zhang, Recent progress in modification and composite strategies of graphitic carbon nitride as catalysts for heterogeneous photo-Fenton reaction, Mater. Sci. Semicond. Process. 167 (2023) 107807.

[14] Z. Xue, M. Yan, Y. Zhang, J. Xu, X. Gao, Y. Wu, Understanding the injection process of hydrogen on Pt1-TiO$_2$ surface for photocatalytic hydrogen evolution, Appl. Catal. B 325 (2023) 122303.

[15] L. Sun, H. Dong, J. Xu, X. Liu, H. Tang, Unravelling the synergy between phase engineering and interface regulation in TiO$_2$/1T-Rich MoSe$_2$ heterostructures for efficient photocatalytic hydrogen evolution, ACS Sustain. Chem. Eng. 11 (2023) 8009–8019.

[16] Z. Wang, J. You, J. Li, J. Xu, X. Li, H. Zhang, Review on cobalt ferrite as photo-Fenton catalysts for degradation of organic wastewater, Catal. Sci. Technol. 13 (2023) 274–296.

[17] C. Wang, P. Shi, Z. Wang, R. Guo, J. You, H. Zhang, Efficient wastewater disinfection through FeOOH-mediated photo-Fenton reaction: A review, J. Environ. Chem. Eng. 11 (2023) 111269.

[18] J. Li, H. Li, G. Zhan, L. Zhang, Solar water splitting and nitrogen fixation with layered bismuth oxyhalides, Acc. Chem. Res. 50 (2017) 112–121.

[19] J. Sharma, P. Dhiman, R.A. Alshgari, Z.A. ALOthman, A. Kumar, G. Sharma, G. Rana, Advances in photocatalytic environmental and clean energy applications of Bismuth-rich oxy halides (Bi$_x$O$_y$X$_z$) based heterojunctions: A review, Mater. Today Sustain 21 (2023) 100327.

[20] J. Li, J. You, Z. Wang, Y. Zhao, J. Xu, M. Duan, H. Zhang, Fe$_2$O$_3$/BiVO$_4$ heterogeneous photo-Fenton catalyst with excellent dye degradation performance prepared by ultrasonic-assisted calcination, J. Mater. Sci. 58 (2023) 10274–10287.

[21] X. Zheng, Y. Song, Y. Liu, Y. Yang, D. Wu, Y. Yang, S. Feng, J. Li, W. Liu, Y. Shen, ZnIn$_2$S$_4$-based photocatalysts for photocatalytic hydrogen evolution via water splitting, Coord. Chem. Rev. 475 (2023) 214898.

[22] W.-K. Chong, B.-J. Ng, X.Y. Kong, L.-L. Tan, L.K. Putri, S.-P. Chai, Non-metal doping induced dual pn charge properties in a single ZnIn$_2$S$_4$ crystal structure provoking charge transfer behaviors and boosting photocatalytic hydrogen generation, Appl. Catal. B 325 (2023) 122372.

[23] Y. Lei, K.H. Ng, Y. Zhu, Y. Zhang, Z. Li, S. Xu, J. Huang, J. Hu, Z. Chen, W. Cai, Mo-activated VC as effective cocatalyst for an enhanced photocatalytic hydrogen evolution activity of CdS, Chem. Eng. J. 452 (2023) 139325.

[24] N. Wang, D. Wang, A. Wu, S. Wang, Z. Li, C. Jin, Y. Dong, F. Kong, C. Tian, H. Fu, Few-layered MoS$_2$ anchored on 2D porous C$_3$N$_4$ nanosheets for Pt-free photocatalytic hydrogen evolution, Nano Res 16 (2023) 3524–3535.

[25] S.-T. Xiao, R. Yin, L. Wu, S.-M. Wu, G. Tian, M. Shalom, L.-Y. Wang, Y.-T. Wang, F.-F. Pu, H.-N. Barad, Hierarchically porous few-layer carbon nitride and its high H$^+$ selectivity for efficient photocatalytic seawater splitting, Nano Lett. 23 (2023) 4390–4398.

[26] X. Wang, Z. Liang, Y. Xue, X. Chen, X. Qian, Y. Zhou, X. Zhang, H. Cui, J. Tian, A novel semi-metallic 1T'-MoReS$_3$ co-catalyst, Chem. Eng. J. 425 (2021) 130525.

[27] C. Cheng, J. Shi, L. Mao, C.-L. Dong, Y.-C. Huang, S. Zong, J. Liu, S. Shen, L. Guo, Ultrathin porous graphitic carbon nitride from recrystallized precursor toward significantly enhanced photocatalytic water splitting, J. Colloid Interface Sci. 637 (2023) 271–282.

[28] W. Shao, F. Zhao, J. Xue, L. Huang, NIR-II absorbing organic nanoagents for photoacoustic imaging and photothermal therapy, BMEMat 1 (2023) e12009.

[29] N. Yang, C. Cao, X. Lv, T. Zhang, J. Shao, X. Song, W. Wang, P. Chen, W. Huang, X. Dong, Photo-facilitated chemodynamic therapeutic agents: Synthesis, mechanisms, and biomedical applications, BMEMat 1 (2023) e12005.

[30] Q. Wu, H. Zhang, H. Liu, External physical field-driven nanocatalytic cancer therapy, BMEMat 1 (2023) e12010.

[31] J. Yu, H. Zhang, Q. Liu, J. Yu, J. Zhu, Y. Li, R. Li, J. Wang, 2D/2D heterojunction of Ti$_3$C$_2$/porous few-layer g-C$_3$N$_4$ nanosheets for high-efficiency extraction of uranium (VI), Sep. Purif. Technol. 312 (2023) 123442.

[32] B. Yang, X. Li, Q. Zhang, X. Yang, J. Wan, G. Liao, J. Zhao, R. Wang, J. Liu, R. D. Rodriguez, X. Jia, Ultrathin porous carbon nitride nanosheets with well-tuned band structures via carbon vacancies and oxygen doping for significantly boosting H$_2$ production, Appl. Catal. B 314 (2022) 121521.

[33] J. Xing, X. Huang, X. Yong, X. Li, J. Li, J. Wang, N. Wang, H. Hao, N-doped synergistic porous thin-walled g-C$_3$N$_4$ nanotubes for efficient tetracycline photodegradation, Chem. Eng. J. 455 (2023) 140570.

[34] B. Yang, J. Han, Q. Zhang, G. Liao, W. Cheng, G. Ge, J. Liu, X. Yang, R. Wang, X. Jia, Carbon defective g-C$_3$N$_4$ thin-wall tubes for drastic improvement of photocatalytic H$_2$ production, Carbon 202 (2023) 348–357.

[35] Y. Wang, X. Yang, T. Tian, Y. Liu, Y. Chen, G. Xu, L. Gu, H. Li, Y. Yuan, Chitosan-assisted synthesis of 1D g-C$_3$N$_4$ nanorods for enhanced photocatalysis, Chem. Commun. 59 (2023) 10528–10531.

[36] C. Zhao, C. Li, M. Chen, T. Niu, Q. Zhao, T. Ni, D. Yan, W. Wu, D. Liu, Effective removal of antineoplastic doxorubicin by 0D Nb$_2$O$_5$ quantum dots embed 3D porous C-doped g-C$_3$N$_4$: Degradation mechanism, pathway and toxicity assessment, Appl. Surf. Sci. 612 (2023) 155861.

[37] X. Wang, Y. Xue, Z. Liang, J. Tian, X. Zhang, X. Chen, Insights into the function of semi-metallic 1T' phase ReS$_2$ as cocatalyst decorated g-C$_3$N$_4$ nanotubes for enhanced photocatalytic hydrogen production activity, Mater. Today Adv. 15 (2022) 100257.

[38] B. Yang, Z. Wang, J. Zhao, X. Sun, R. Wang, G. Liao, X. Jia, 1D/2D carbon-doped nanowire/ultra-thin nanosheet g-C$_3$N$_4$ isotype heterojunction for effective and durable photocatalytic H$_2$ evolution, Int. J. Hydrog. Energy 46 (2021) 25436–25447.

[39] Z. Li, T. Sun, G. Zhang, Combining heterogeneous photocatalysis and enzymatic catalysis via membrane: Conversion of biomass for H$_2$ production from water, Appl. Catal. B 338 (2023) 123069.

[40] S. Gao, X. Guo, K. Liu, Y. Li, T. Li, X. Gu, R. Arenal, X. Zheng, W. Li, C. Sun, Size effect of CoS$_2$ cocatalyst on photocatalytic hydrogen evolution performance of g-C$_3$N$_4$, J. Colloid Interface Sci. 635 (2023) 305–315.

[41] P.A. Nguyen, Q.D. Dao, T.T. Dang, T.V.A. Hoang, J.S. Chung, E.W. Shin, Highly dispersed PtO over g-C$_3$N$_4$ by specific metal-support interactions and optimally distributed Pt species to enhance hydrogen evolution rate of Pt/g-C$_3$N$_4$ photocatalysts, Chem. Eng. J. 464 (2023) 142765.

[42] K. Huang, C. Lv, C. Li, H. Bai, X. Meng, Ti$_3$C$_2$ MXene supporting platinum nanoparticles as rapid electrons transfer channel and active sites for boosted photocatalytic water splitting over g-C$_3$N$_4$, J. Colloid Interface Sci. 636 (2023) 21–32.

[43] H.S. Moon, K.C. Hsiao, M.C. Wu, Y. Yun, Y.J. Hsu, K. Yong, Spatial separation of cocatalysts on Z-scheme organic/inorganic heterostructure hollow spheres for enhanced photocatalytic H$_2$ evolution and in-depth analysis of the charge-transfer mechanism, Adv. Mater. 35 (2023) 2200172.

[44] X. Xiang, L. Zhang, C. Luo, J. Zhang, B. Cheng, G. Liang, Z. Zhang, J. Yu, Ultrafast electron transfer from CdS quantum dots to atomically-dispersed Pt for enhanced H$_2$ evolution and value-added chemical synthesis, Appl. Catal. B 340 (2024) 123196.

[45] G. Zhang, Y. Xu, J. Zhu, Y. Li, C. He, X. Ren, P. Zhang, H. Mi, Enhanced photocatalytic H$_2$ production independent of exciton dissociation in crystalline carbon nitride, Appl. Catal. B 338 (2023) 123049.

[46] R. Cao, H. Yuan, N. Yang, Q. Lu, Y. Xue, X. Zeng, Enhanced photocatalytic hydrogen production utilizing few-layered 1T-WS$_2$/g-C$_3$N$_4$ heterostructures prepared with one-step calcination route, Fuel 357 (2024) 129808.

[47] S. Higgins, Regarding ruthenium, Nat. Chem. 2 (2010) 1100.

[48] Y. Li, L.A. Zhang, Y. Qin, F. Chu, Y. Kong, Y. Tao, Y. Li, Y. Bu, D. Ding, M. Liu, Crystallinity dependence of ruthenium nanocatalyst toward hydrogen evolution reaction, ACS Catal. 8 (2018) 5714–5720.

[49] J. Yu, Q. He, G. Yang, W. Zhou, Z. Shao, M. Ni, Recent advances and prospective in ruthenium-based materials for electrochemical water splitting, ACS Catal. 9 (2019) 9973–10011.

[50] Y. Zheng, Y. Jiao, Y. Zhu, L.H. Li, Y. Han, Y. Chen, M. Jaroniec, S.-Z. Qiao, High electrocatalytic hydrogen evolution activity of an anomalous ruthenium catalyst, J. Am. Chem. Soc. 138 (2016) 16174–16181.

[51] W. Li, Y. Liu, M. Wu, X. Feng, S.A. Redfern, Y. Shang, X. Yong, T. Feng, K. Wu, Z. Liu, Carbon-quantum-dots-loaded ruthenium nanoparticles as an efficient electrocatalyst for hydrogen production in alkaline media, Adv. Mater. 30 (2018) 1800676.

[52] J. Liu, G. Ding, J. Yu, X. Liu, X. Zhang, J. Guo, J. Zhang, W. Ren, R. Che, Visualizing spatial potential and charge distribution in Ru/N-doped carbon electrocatalysts for superior hydrogen evolution reaction, J. Mater. Chem. A 7 (2019) 18072–18080.

[53] Z. Peng, Z. Wang, L. Zhou, Y. Wang, J. Gao, G. Liu, S.A. Redfern, X. Feng, S. Lu, B. Li, Hollow carbon shells enhanced by confined ruthenium as cost-efficient and superior catalysts for the alkaline hydrogen evolution reaction, J. Mater. Chem. A 7 (2019) 6676–6685.

[54] X. Sun, X. Gao, J. Chen, X. Wang, H. Chang, B. Li, D. Song, J. Li, H. Li, N. Wang, Ultrasmall Ru nanoparticles highly dispersed on sulfur-doped graphene for HER with high electrocatalytic performance, ACS Appl. Mater. Interfaces 12 (2020) 48591–48597.

[55] M. Tan, Y. Wang, A. Taguchi, T. Abe, G. Yang, M. Wu, N. Tsubaki, Highly-dispersed Ru nanoparticles sputtered on graphene for hydrogen production, Int. J. Hydrog. Energy 44 (2019) 7320–7325.

[56] S. Ye, F. Luo, T. Xu, P. Zhang, H. Shi, S. Qin, J. Wu, C. He, X. Ouyang, Q. Zhang, Boosting the alkaline hydrogen evolution of Ru nanoclusters anchored on B/N–doped graphene by accelerating water dissociation, Nano Energy 68 (2020) 104301.

[57] J. Liu, Y. Zheng, D. Zhu, A. Vasileff, T. Ling, S.-Z. Qiao, Identification of pH-dependent synergy on Ru/MoS$_2$ interface: a comparison of alkaline and acidic hydrogen evolution, Nanoscale 9 (2017) 16616–16621.

[58] U. Joshi, S. Malkhandi, Y. Ren, T.L. Tan, S.Y. Chiam, B.S. Yeo, Ruthenium–tungsten composite catalyst for the efficient and contamination-resistant electrochemical evolution of hydrogen, ACS Appl. Mater. Interfaces 10 (2018) 6354–6360.

[59] J. Yu, Y. Guo, S. Miao, M. Ni, W. Zhou, Z. Shao, Spherical ruthenium disulfide-sulfur-doped graphene composite as an efficient hydrogen evolution electrocatalyst, ACS Appl. Mater. Interfaces 10 (2018) 34098–34107.

[60] P. Li, X. Duan, S. Wang, L. Zheng, Y. Li, H. Duan, Y. Kuang, X. Sun, Amorphous ruthenium-sulfide with isolated catalytic sites for Pt-like electrocatalytic hydrogen production over whole pH range, Small 15 (2019) 1904043.

[61] Y. Li, J. Li, J. Chen, P. Cai, G. Wang, Y. Hou, L. Lei, Z. Wen, RuS$_{2-x}$ quantum dots/rGO as bifunctional hydrogen electrocatalysts for harvesting electrochemical neutralization energy, J. Power Sources 472 (2020) 228625.

[62] Y. Xia, W. Wu, H. Wang, S. Rao, F. Zhang, G. Zou, Amorphous RuS$_2$ electrocatalyst with optimized active sites for hydrogen evolution, Nanotechnology 31 (2020) 145401.

[63] Y. Zhu, H.A. Tahini, Y. Wang, Q. Lin, Y. Liang, C.M. Doherty, Y. Liu, X. Li, J. Lu, S. C. Smith, Pyrite-type ruthenium disulfide with tunable disorder and defects enables ultra-efficient overall water splitting, J. Mater. Chem. A 7 (2019) 14222–14232.

[64] J. Zhu, Y. Guo, F. Liu, H. Xu, L. Gong, W. Shi, D. Chen, P. Wang, Y. Yang, C. Zhang, Regulative electronic states around ruthenium/ruthenium disulphide heterointerfaces for efficient water splitting in acidic media, Angew. Chem. 133 (2021) 12436–12442.

[65] M. Cheng, H. Geng, Y. Yang, Y. Zhang, C.C. Li, Optimization of the hydrogen-adsorption free energy of Ru-based catalysts towards high-efficiency hydrogen evolution reaction at all pH, Chem. Eur. J. 25 (2019) 8579–8584.

[66] X. Gao, B. Li, X. Sun, B. Wu, Y. Hu, Z. Ning, J. Li, N. Wang, Engineering heterostructure and crystallinity of Ru/RuS$_2$ nanoparticle composited with N-doped graphene as electrocatalysts for alkaline hydrogen evolution, Chin. Chem. Lett. 32 (2021) 3591–3595.

[67] J. Wang, Q. Fan, L. Kou, H. Chen, X. Xing, W. Duan, K. Jiang, LED-driven sulfamethazine removal and bacterial disinfection by a novel photocatalytic textile

impregnated with oxygen vacancy-rich BiO_{2-x}/g-C_3N_4 hybrid, Chem. Eng. J. 474 (2023) 145590.

[68] J. Gu, C. Ban, J. Meng, Q. Li, X. Long, X. Zhou, N. Liu, Z. Li, Construction of dual Z-scheme UNiMOF/$BiVO_4$/S-C_3N_4 photocatalyst for visible-light photocatalytic tetracycline degradation and Cr (VI) reduction, Appl. Surf. Sci. 611 (2023) 155575.

[69] H.A. Omr, R. Putikam, M.K. Hussien, A. Sabbah, T.-Y. Lin, K.-H. Chen, H.-L. Wu, S.-P. Feng, M.-C. Lin, H. Lee, Design of sculptured SnS/g-C_3N_4 photocatalytic nanostructure for highly efficient and selective CO_2 conversion to methane, Appl. Catal. B 324 (2023) 122231.

[70] Z.-Y. Fu, H.-M. Xu, W.-H. Li, G.-P. Jin, S.-K. Han, Phase transformation from amorphous RuS_x to Ru-RuS_2 hybrid nanostructure for efficient water splitting in alkaline media, Inorg. Chem. 62 (2022) 583–590.

[71] Q. Liu, Z. Chen, W. Tao, H. Zhu, L. Zhong, F. Wang, R. Zou, Y. Lei, C. Liu, X. Peng, Edge activation of an inert polymeric carbon nitride matrix with boosted absorption kinetics and near-infrared response for efficient photocatalytic CO_2 reduction, J. Mater. Chem. A 8 (2020) 11761–11772.

[72] T. Mahvelati-Shamsabadi, K.C. Bhamu, S.-h Lee, T.T. Dang, V.H. Khoi, S.H. Hur, W. M. Choi, S.G. Kang, T.J. Shin, J.S. Chung, Coordinatively unsaturated atomically dispersed Pt^{+2}-N_4 sites on hexagonal nanosheet structure of g-C_3N_4 for high-performance photocatalytic H_2 production, Appl. Catal. B (2023) 122959.

[73] D. Liu, J. Yao, S. Chen, J. Zhang, R. Li, T. Peng, Construction of rGO-coupled C_3N_4/C_3N_5 2D/2D Z-scheme heterojunction to accelerate charge separation for efficient visible light H_2 evolution, Appl. Catal. B 318 (2022) 121822.

[74] F. Gao, H. Xiao, J. Yang, X. Luan, D. Fang, L. Yang, J. Zi, Z. Lian, Modulation of electronic density in ultrathin g-C_3N_4 for enhanced photocatalytic hydrogen evolution through an efficient hydrogen spillover pathway, Appl. Catal. B 341 (2024) 123334.

[75] M. Yang, P. Wang, Y. Li, S. Tang, X. Lin, H. Zhang, Z. Zhu, F. Chen, Graphene aerogel-based NiAl-LDH/g-C_3N_4 with ultratight sheet-sheet heterojunction for excellent visible-light photocatalytic activity of CO_2 reduction, Appl. Catal. B 306 (2022) 121065.

[76] Y. Guo, S. Huang, Y. Guo, Z. Ye, J. Nan, Q. Zhou, Y. Zhu, Efficient degradation of organic pollutants by enhanced interfacial internal electric field induced via various crystallinity carbon nitride homojunction, Appl. Catal. B 312 (2022) 121388.

[77] J. Ning, Y. Chen, T. Wang, J. Xiong, In-situ fabrication of Ru/C_3N_4 nanosheets Mott-Schottky photocatalyst for enhanced photocatalytic H_2 evolution, Int. J. Electrochem. Sci. 17 (2022) 220855.

[78] Y. Liu, Y. Li, X. Li, Q. Zhang, H. Yu, X. Peng, F. Peng, Regulating electron–hole separation to promote photocatalytic H_2 evolution activity of nanoconfined Ru/MXene/TiO_2 catalysts, ACS Nano 14 (2020) 14181–14189.

[79] M. Humayun, Q. Fu, Z. Zheng, H. Li, W. Luo, Improved visible-light catalytic activities of novel Au/P-doped g-C_3N_4 photocatalyst for solar fuel production and mechanism, Appl. Catal. A: Gen. 568 (2018) 139–147.

[80] M. Liu, P. Xia, L. Zhang, B. Cheng, J. Yu, Enhanced photocatalytic H_2-production activity of g-C_3N_4 nanosheets via optimal photodeposition of Pt as cocatalyst, ACS Sustain. Chem. Eng. 6 (2018) 10472–10480.

[81] H. Li, Y. Wu, C. Li, Y. Gong, L. Niu, X. Liu, Q. Jiang, C. Sun, S. Xu, Design of Pt/t-ZrO_2/g-C_3N_4 efficient photocatalyst for the hydrogen evolution reaction, Appl. Catal. B 251 (2019) 305–312.

[82] S. Li, Y. Peng, C. Hu, Z. Chen, Self-assembled synthesis of benzene-ring-grafted g-C_3N_4 nanotubes for enhanced photocatalytic H_2 evolution, Appl. Catal. B 279 (2020) 119401.

[83] Y. Zhu, T. Wan, X. Wen, D. Chu, Y. Jiang, Tunable Type I and II heterojunction of CoO_x nanoparticles confined in g-C_3N_4 nanotubes for photocatalytic hydrogen production, Appl. Catal. B 244 (2019) 814–822.

[84] K. Li, Z. Zeng, L. Yan, S. Luo, X. Luo, M. Huo, Y. Guo, Fabrication of platinum-deposited carbon nitride nanotubes by a one-step solvothermal treatment strategy and their efficient visible-light photocatalytic activity, Appl. Catal. B 165 (2015) 428–437.